12

Measurements of Particle Velocities and Trajectories for Internal Waves Propagating in a Density-Stratified Two-Layer Fluid on a Slope

Motohiko Umeyama, Tetsuya Shintani,
Kim-Cuong Nguyen and Shogo Matsuki
Department of Civil & Environmental Engineering, Tokyo Metropolitan University
Japan

1. Introduction

The existence of internal waves was first recognized by a measurement of water temperature by Helland-Hansen and Nansen (1926). Later, the vertical structure of internal waves has been detected by observation of temperature, salinity, or ocean current, while the propagation of internal waves has been identified by images from radar or acoustic Doppler and echo sounder. Shand (1953) found internal wave fronts appearing on aerial photographs. From observation of offshore temperature variations, LaFond (1962) found that time-dependent isotherms are flattened for a shallower thermocline and peaked for a deeper thermocline on the wave crests. Apel et al. (1975, 1976, 1985) reported a series of research results for the internal waves observed in pictures from satellites, space shuttles, and aircraft. In addition to these indirect photographs, they also used various instruments such as the expendable bathythermograph (XBT), acoustic echo sounding, and ship radar.

In contrast, numerous researchers have carried out laboratory experiments to examine the shoaling and breaking of internal waves on various topographic features. Thorpe (1968) studied the breaking and runup of internal waves in a two-layered system, and found that internal waves steepen at the front as the lower layer becomes shallow, but the crests break backwards unlike surface breakers. On the upper slope, the wave (bolus) behaves like the front of a gravity current, and the dense fluid returning down the slope from previous waves flows over the top of the overcoming waves. Using a hydrogen-bubble wiring system, Kao et al. (1985) measured the particle velocity profile during the passage of internal waves. Wallace and Wilkinson (1988) found that overturning is initiated by the interaction of an incident wave with the backflow from the preceding boluses. Helfrich (1992) performed experiments to observe the interaction of an internal wave of depression with a sloping bottom, and recognized the importance of the backflow that produces significant mixing. He found a rapid offshore flow of lower-layer water while the front face of the incident wave moved up the slope.

There have been significant developments in measuring fluid velocities by using laboratory equipment, but the use of tools such as the electric–magnetic current meter and laser Doppler anemometer has not solved kinetic problems for internal waves. Experimental studies for fluid

velocities have generally relied on point measurement techniques. However, recent advances in technology provide two and three–dimensional features of the velocity field for several flow problems. Visualization techniques have played an essential role in fluid flows during the previous decade, because they yield both qualitative and quantitative insights in geophysical or environmental fluid mechanics. Now, imaging techniques enable high–resolution images of several kinds of unsteady flows. The latest developments in particle image velocimetry (PIV) and particle tracking velocimetry (PTV) have led to the visualization of velocity fields and particle paths. Both techniques are analysis methods for image pairs taken in a seeded flow field with known temporal separation. Water velocities due to the propagation of internal waves have been measured by Michallet and Ivey (1999), and Walker et al. (2003) using PIV, and by Grue et al. (1999, 2000) using PTV.

The mechanism of internal waves in a two-layer system comprising homogeneous fluids of slightly different densities has been studied using visualization techniques in the Hydraulic Laboratory at Tokyo Metropolitan University. In the research of Umeyama (2002), a digital video camera was first used to illustrate the internal waves propagating in a fluid of finite depth over a flat bed. After analysing continuous pictures recorded on a DV tape, the density interface was determined from a set of luminance values using image-processing software. The temporal and spatial variations of the density interface were compared with the analytical results based on the third-order finite amplitude approximation. Umeyama and Shintani (2004) installed a Plexiglas plate in the same wave tank to observe the runup and breaking of long internal waves over an artificial slope. The profile of internal waves and the mixing between upper and lower layers, were visualized by adding a blue dye (Anilin Blue) in lower salt water. Later, Umeyama and Shintani (2006) performed more precise laboratory tests, by considering additional aspects such as transformation, attenuation, set-down, and setup during the shoaling and breaking events. The method of characteristics, energy dissipation model with radiation stress, and momentum balance equation were used to confirm the experimental results. To study the transformation processes using instantaneous and mean velocity fields and nonlinear properties using interfacial displacements over a uniform slope, Shimizu et al. (2005) developed a PIV system that consisted of a Nd:YAG pulsed laser and a CCD camera. The analysis, however, highlighted the limitations in the measuring range. This PIV system of the laser sheet could not measure a large area while maintaining a fine resolution. The PIV measurements were repeated three times to cover one wavelength and the total depth in adjoining areas for each case. In contrast, Umeyama (2008) and Umeyama and Shinomiya (2009) developed a new PIV system that utilized halogen lamps and three high-definition digital video cameras in which the maximum resolution was 2,016×1,134 pixels and the images were recorded on a hard disk. Each video camera, operating simultaneously side by side, covered a larger area with a frame rate 16:9. Since the water surface was almost flat during all experiments, the halogen lamps were set in a line along the wave tank at its top, and the light sheet of 3 mm width was emitted from the upper side of the wave tank. Umeyama and Matsuki (2011) recently measured the similar physical quantities with two frequency-doubled Nd:YAG lasers of 50 mW energy at 532 nm as the illumination sources. In addition to the common use of the PIV technique, the knowledge has been extended to visualize water particle paths and mass transport variations due to the propagation of internal waves in the tank.

From a Eulerian prospective, the motion of an incompressible fluid is distinctive if the velocity vectors occupy an instantaneous velocity field. As PIV is used to represent a regular

array of velocity vectors, it is convenient to define the Eulerian velocity based upon the average particle motion in the possible space. In contrast, PTV traces the individual particle path from a sequence of images in a system. From a Lagrangian viewpoint, PTV is better suited than PIV for handling unsteady flow. Quantitative results for Lagrangian fluid motion can be obtained through computerized analyses of the particle images in the modern PTV technique. Generally, PIV has determined the Eulerian velocity field from a sequence of images, while PTV has estimated the Lagrangian velocity by tracing individual particle paths. Umeyama (2011) employed a PTV system with single-exposure images to track particle displacements for surface waves with or without a steady current. In addition to the basic use of PTV, an alternative measurement technique was proposed to describe particle trajectories in a Eulerian scheme through PIV analysis. Later, Umeyama et al. (2011) made similar measurement and analysis for the water particle velocity and trajectory using a PIV system with two Nd:YAG lasers of 50 mW. In this experiment, DIAION and micro bubbles were chosen as tracer. More recently, Umeyama (2012) measured the water particle velocity and trajectory in a pure wave motion using a new PIV system with an 8 W Nd:YAG laser. These previous validation results are presented by comparing the measurements of the PIV system to those of the electromagnetic current (EC) meter.

This article investigates the spatial and temporal variations of the density interface, wave height, celerity and setup due to shoaling and breaking of internal waves, using an image processing technique, and the velocity and trajectory of water particles in an internal wave motion, using particle image velocimetry (PIV). The writers illustrate 2D instantaneous displacements of density interface from the observed data, and analyse them to obtain the wave height, celerity, and setup. These results are compared with the calculated values by the method of characteristics, the simple shoaling model with energy dissipation, and the momentum balance equation based on a radiation stress concept. The vector fields and vertical distributions of velocities are presented at several phases in one wave cycle. The PIV technique's ability to measure both temporal and spatial variations of the velocity is proven after a series of attempts. This technique is applied to the prediction of particle trajectory in a Eulerian scheme. The measured particle path is compared to the positions found theoretically by the method of characteristics.

2. Experiments and data analysis

2.1 Wave tank and wavemakers

Experiments on internal waves were carried out in the 6.0-m-long, 0.15-m-wide, and 0.35-m-deep wave tank. It was constructed of 12 Plexiglas panels, 10 stainless flanges, and a stainless bottom. Each glass panel was 91.0 cm long, 27.0 cm high and 1.0 cm thick. A wave generator was placed at one end. Fig. 1 shows a sketch of the apparatus for the wave tank and its photograph.

In the earlier stages of experiments, Umeyama (2002) and Umeyama & Shintani (2004, 2006) used a horizontal flap-type wavemaker. Recently, experimental studies were undertaken to test several types of wave-generating paddles, and a different kind of wavemaker was set at one end of the wave tank. The sketch of the new wavemaker is presented in Fig.2. This slide-type wavemaker consists of a D-shaped paddle and a linear actuator that moves smoothly and programmatically within a given stroke length. As the D-shaped paddle limits the mixing of the upper and lower waters, the intermediate density layer does not grow quickly

during each test. Umeyama (2008), Umeyama & Shinomiya (2009), and Umeyama & Matsuki (2011) examined internal waves generated by the slide-type wavemaker to obtain insight into the nonlinear properties and kinematics.

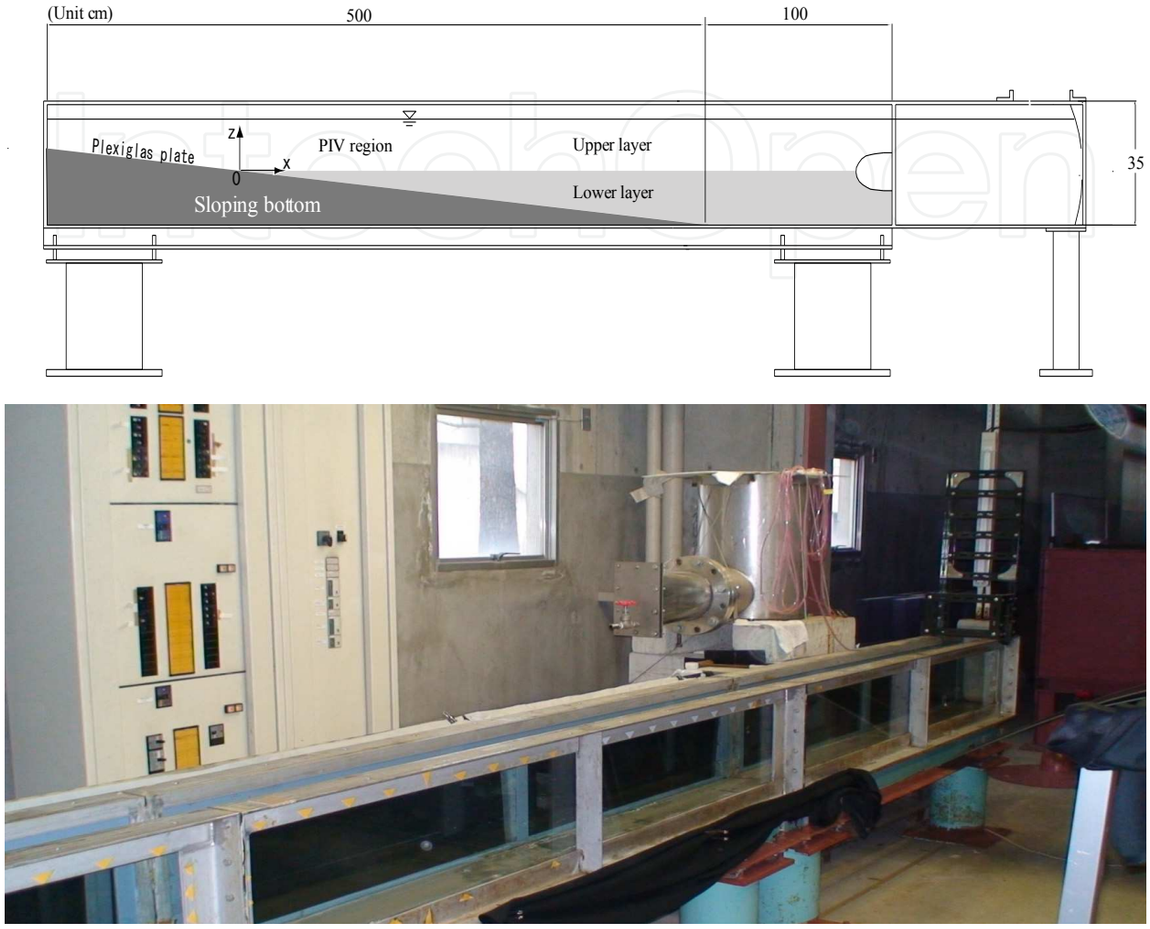

Fig. 1. A schematic diagram of experimental arrangements and a photograph of wave tank

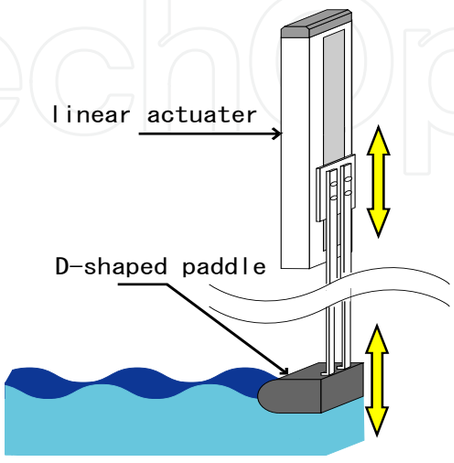

Fig. 2. A slide-type wavemaker with a D-shaped paddle

In the present study, a 1-cm-thick Plexiglas plate, which served as the plane seabed, was fabricated between 100 and 600 m from the wavemaker. A density-stratified fluid consisting of fresh water and salt water was prepared for the experiments, and the density of the salt water was 1,030 mg/cm^3. The total water depth from the bottom of the wave tank was kept at 30 cm. The density of the salt water was assumed to be constant initially, but subsequent disturbances produced deviations from the original density value.

2.2 Flow visualization

Using an image processing technique, Umeyama & Shintani (2004) illustrated the temporal and spatial variations of the density interface and the mixture of upper and lower layer waters in the density-stratified two-layer fluid on a sloping bed. The numerically predicted density variation due to mixing was compared with a set of luminance data analyzed by the image processing technique. Later, Umeyama & Shintani (2006) and Umeyama (2008) extended the aspects of internal wave mechanics during shoaling and breaking events. The objective of these studies was to observe internal waves approaching an upper slope in a wave tank using a video recording system, convert the measured data to the wave profile, celerity, height and setup, and compare the experimental values with theoretical ones. For the flow visualization and video recording technique in detail, refer to Umeyama (2008). The colour image file from the video recorder was transferred to an 8-bit (256 grades) grayscale image file. Using the method of image segmentation, individual pixels in a grayscale image were marked as object or background pixels. The density interface was estimated from the spatial distribution of the threshold. Finally, the temporal displacements of the density interface were obtained at several points, and the wave height and mean level were estimated by averaging these displacements about 10 wave periods. This duration may be assumed stationary at the location where data are gathered, because artificial internal waves are considered approximately stationary only for a few minutes. Beyond the duration, their properties are expected to change in the wave tank.

An internal wave gauge was also used to measure the vertical displacement of density interface at a location 100 cm from the wave maker. A salinity sensor at the tip of the internal wave gauge could run after the position of the prescribed salt density layer. Under each set of experimental conditions, experimental data were collected continuously at a frequency of 47 Hz.

2.3 PIV technique

The instantaneous water particle velocities induced by internal waves were measured using PIV. The basic principle of PIV is evaluating the instantaneous velocities through recording the position of images of small tracers, suspended in the fluid, at successive instants in time. In practice, when two successive images of tracers illuminated in a thin and intense light sheet are acquired, the velocity is calculated from the known time difference and measured displacement.

In this study, the water particle velocity was measured using a single-exposure image PIV system. The instantaneous vector field was trapped in the 91-cm-long and 27-cm-high glass panel using a frequency-doubled Nd:YAG laser of 8-W energy at 532 nm. A 2-mm-thick light sheet was emitted from the upper side: this light sheet had a very uniform

intensity and covered the total area in the glass panel. The system included two high-definition digital video cameras (SONY HXR-NX5J) with a maximum resolution of 1920×1080 pixels. The video camera was arranged linearly 1.28 m from the sidewall of the wave tank. The camera image area was centered in the light sheet; consequently, the corresponding viewing area up to 100.0 cm×28.0 cm was chosen using the optical arrangement. According to Austin and Halikas (1976), the index of refraction of clear water is 1.335, while that of salt water with a density of 1,030 mg/cm^3 is 1.341. As the index of refraction varies by less than 0.5% (the maximum difference in angle of refraction is approximately 0.1 degree), the difference in geometric distortion was not corrected. DIAION (DK-FINE HP20SS) was used to capture the high-contrast images with the particle tracer in both layers. It consisted of ion-exchange resin with the homogeneous matrix structure inside the particle. This kind of matrix gave micropores formed by the polymeric networks, so that water could pass through these pores. Before each experiment, DIAION was mixed in the salt water. Analysis of the displacement of images in each interrogation window by means of the cross-correlation method leads to an estimated average displacement of particles. The resolution is directly related to the size of the interrogation window. The displacement vector computed at any location is the spatially averaged transitional motion of particles. Vector fields could be obtained with the PIV system processing a pair of images, using an interrogation window of 64×64 pixels in a candidate region of 128×128 pixels. Since the internal wave topography does not change significantly over 0.1 s, the resultant displacement of topographic features for two images spaced in Δt =0.1 s was chosen for a direct calculation of the velocity vectors.

2.4 Eulerian/Lagrangian method

A cross-correlation method was performed to calculate the water particle displacement and local velocity by processing a pair of image frames. Although the representation of the velocity vector field in a Eulerian system is a typical example of the PIV method, the result can be applied to a particle tracking process in a Lagrangian system. Umeyama & Matsuki (2011) used the velocity given at the spatially discrete nodal point to estimate the imaginary velocity and location of a particle.

The following explains the particle motion within a tracking time step Δt along an arbitrary trajectory across a general mesh of quadrilateral cells (Fig.3). The algorithm has two steps: (1) the velocity value of a Lagrangian point A where t is obtained by interpolating the neighboring velocity values (u_1 at P_1, u_2 at P_2, u_3 at P_3, and u_4 at P_4, where P_1, P_2, P_3, and P_4 are corners of the mesh), and (2) the particle associated with the Lagrangian point at t is traced to a hypothetical location (A') at $t+\Delta t$. Thus, these Lagrangian velocities u_L at t and u_L' at $t+\Delta t$ are

$$u=\frac{\frac{u_1}{l_1}+\frac{u_2}{l_2}+\frac{u_3}{l_3}+\frac{u_4}{l_4}}{\frac{1}{l_1}+\frac{1}{l_2}+\frac{1}{l_3}+\frac{1}{l_4}} \text{ at } t=t, \text{ and } u'=\frac{\frac{u_1'}{l_1'}+\frac{u_2'}{l_2'}+\frac{u_3'}{l_3'}+\frac{u_4'}{l_{14}'}}{\frac{1}{l_1'}+\frac{1}{l_2'}+\frac{1}{l_3'}+\frac{1}{l_4'}} \text{ at } t=t+\Delta t$$

where l_1, l_2, l_3, l_4, l_1', l_2', l_3', and l_4' are distances to the imaginary location of a particle from the Eulerian grid points.

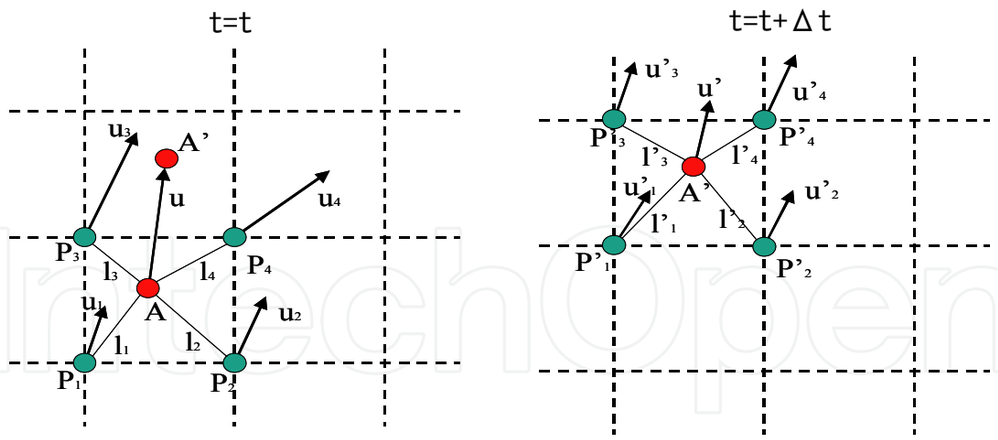

Fig. 3. Lagrangian particle trajectory on Eulerian grids

2.5 Experimental conditions

The experimental conditions are listed in Table 1 that includes the present results in the Hydraulic Laboratory of Tokyo Metropolitan University.

Case	Slope	Density	h_I:h_{II}	Wave height*	Wave period
1	3/50	1,030 mg/cm^3	15 cm:15 cm	2.6 cm	5.2 s
2				2.7 cm	7.2 s
3	3/50	1,030 mg/cm^3	10 cm:20 cm	2.8 cm	5.2 s
4				2.4 cm	7.2 s

* Wave height was measured using wave gauge at 100 cm from the wavemaker.

Table 1. Experimental cases

3. Theory

3.1 Stokes internal waves

First, we consider Stokes internal waves propagating along the interface between two homogeneous incompressible and inviscid fluids of different density in a constant depth. The origin of the axes is located in the undisturbed interface. The density and depth of the upper layer are ρ_I and h_I, respectively, and those of the lower layer are ρ_{II} and h_{II}, respectively. The vertical displacements of the free surface and the density interface are $\eta_I(x,t)$ and $\eta_{II}(x,t)$, respectively. Let $\phi_I(x,z,t)$, and $\phi_{II}(x,z,t)$ denote the velocity potentials in the upper and lower layers, so that the Laplace equations are

$$\phi_{Ixx} + \phi_{Izz} = 0 \tag{1}$$

$$\phi_{IIxx} + \phi_{IIzz} = 0 \tag{2}$$

where x =horizontal coordinate; and z =vertical coordinate. The kinematical and dynamical boundary conditions at the free surface are

$$g(\eta_I + h_I) + \phi_{It} + \frac{1}{2}(\phi_{Ix}^2 + \phi_{Iz}^2) = 0 \text{ on } z = h_I + \eta_I \tag{3}$$

$$\eta_{It} + \eta_{Ix}\phi_{Ix} - \phi_{Iz} = 0 \text{ on } z = h_I + \eta_I \tag{4}$$

where g = gravity acceleration; and t = time. The boundary conditions at the density interface are

$$\eta_{IIt} + \eta_{IIx}\phi_{Ix} - \phi_{Iz} = 0 \text{ on } z = \eta_{II} \tag{5}$$

$$\eta_{IIt} + \eta_{IIx}\phi_{IIx} - \phi_{IIz} = 0 \text{ on } z = \eta_{II} \tag{6}$$

$$\rho_I\{g\eta_{II} + \phi_{It} + \frac{1}{2}(\phi_{Ix}^2 + \phi_{Iz}^2)\} = \rho_{II}\{g\eta_{II} + \phi_{IIt} + \frac{1}{2}(\phi_{IIx}^2 + \phi_{IIz}^2)\} \text{ on } z = \eta_{II} \tag{7}$$

The bottom boundary condition is

$$\phi_{IIz} = 0 \text{ on } z = -h_{II} \tag{8}$$

In the finite-amplitude wave theory, the perturbation method is used to solve the above basic equations and boundary conditions. These solutions have been obtained to the second order by Umeyama (1998), and to the third order by Umeyama (2000).

When the displacement of fluid interface is given by a linear profile such as $\eta_{II}(x,t) = a\cos(kx - \sigma t)$, the horizontal and vertical velocity components for the water particle can be obtained from the velocity potentials where $u_I = -\partial\phi_I / \partial x$, $w_I = -\partial\phi_I / \partial z$, $u_{II} = -\partial\phi_{II} / \partial x$, and $w_{II} = -\partial\phi_{II} / \partial z$. Therefore, the velocity components in both layers are expressed as

$$u_I = \frac{ak}{\sigma}(\alpha\cosh kz - \frac{\sigma^2}{k}\sinh kz)\cos(kx - \sigma t) \tag{9}$$

$$w_I = -\frac{ak}{\sigma}(\alpha\sinh kz - \frac{\sigma^2}{k}\cosh kz)\sin(kx - \sigma t) \tag{10}$$

$$u_{II} = -\frac{a\sigma}{\sinh kh_{II}}\cosh k(z + h_{II})\cos(kx - \sigma t) \tag{11}$$

$$w_{II} = \frac{a\sigma}{\sinh kh_{II}}\sinh k(z + h_{II})\sin(kx - \sigma t) \tag{12}$$

where a =amplitude of internal waves; k =wave number; and α =constant that is given by

$$\alpha = \frac{\rho_{II} - \rho_I}{\rho_I}g - \frac{\rho_{II}}{\rho_I}\frac{\sigma^2}{k}\coth kh_{II}$$

The dispersion relation may be written as

$$\sigma^4(\coth kh_I \coth kh_{II} + \frac{\rho_I}{\rho_{II}}) - \sigma^2(\coth kh_I + \coth kh_{II})gk + \frac{\rho_{II} - \rho_I}{\rho_I}(gk)^2 = 0 \tag{13}$$

Solving Eq.(13) for $C = \sigma / k$ and assuming $\rho_{II} \approx \rho_I$, it becomes

$$C = \varepsilon_g \sqrt{\frac{1}{k(\coth kh_I + \coth kh_{II})}} \tag{14}$$

where $\varepsilon_g = \sqrt{\frac{\rho_{II} - \rho_I}{\rho_I} g}$.

Thus the group velocity for internal waves is given by

$$C_g = \frac{C}{2}\left(1 + \frac{\frac{kh_I}{\sinh^2 kh_I} + \frac{kh_{II}}{\sinh^2 kh_{II}}}{\coth kh_I + \coth kh_{II}}\right) \tag{15}$$

3.2 The method of characteristics for long internal waves on a slope

Umeyama and Shintani (2004) investigated the runup of internal waves on a plane impermeable slope. A reliable solution for the displacement of the density interface and the horizontal velocity of the internal waves was derived by means of the method of characteristics. Let $u_{II}(x,z,t)$ denotes the horizontal velocity for long internal waves so that the governing equations are

$$2(1 + \frac{\eta_{II} + h_{II}}{h_I})C_t + u_{IIx}C + 2(1 + \frac{\eta_{II} + h_{II}}{h_I})C_x = 0 \tag{16}$$

$$u_{IIt} + u_{II}u_{IIx} + 2(1 + \frac{\eta_{II} + h_{II}}{h_I})^2 CC_x = g\frac{\rho_{II} - \rho_I}{\rho_{II}}h_{IIx} \tag{17}$$

It is convenient to define the lower-layer thickness for a uniform slope as

$$h_{II} = h_{II}(x) = m\frac{\rho_I}{g(\rho_{II} - \rho_I)}x$$

where m =constant. By adding and subtracting Eqs.(16) and (17), and assuming $\eta + h_{II} << h_I$, the results can be written in the familiar form:

$$[\frac{\partial}{\partial t} + (u_{II} \pm C)\frac{\partial}{\partial x}](u_{II} \pm 2C - mt) = 0 \tag{18}$$

Use of the method of characteristics will make it possible to describe η_{II} and u_{II} such as

$$\eta_{II} = -\frac{A^2}{2}\frac{h_I + sx}{h_I sx}[J_1(X)\cos T + \{J_0(X) - \frac{J_1(X)}{X}\}\sin T]^2 + A\{J_0(X)\sin T + J_1(X)\cos T\} \tag{19}$$

$$u_{II} = A\varepsilon_g \sqrt{\frac{h_I + sx}{h_I sx}} [J_1(X)\cos T + \{J_0(X) - \frac{J_1(X)}{X}\}\sin T] \tag{20}$$

where A =constant; and J_p =the Bessel function of order p. The dependent variables are given by

$$X = \frac{2\sigma}{s\varepsilon_g}\sqrt{\frac{h_I sx}{h_I + sx}}, \text{ and } \quad T = -\sigma t$$

For convenience, the dependent variable X will not be shown hereafter.

A displacement of the interface will cause an associated surface displacement. In the upper layer, the linearized momentum equation may be simply given by

$$\frac{\partial u_I}{\partial t} = -g\frac{\partial \eta_I}{\partial x} \tag{21}$$

The continuity equation can be determined in the same manner:

$$u_I = \frac{C(\eta_I - \eta_{II})}{h_I + (\eta_I - \eta_{II})} \approx -\frac{C}{h_I}\eta_{II} \tag{22}$$

Combining Eqs.(21) and (22), the following differential results:

$$\begin{aligned} \eta_I = &-\frac{A^2\sigma C}{g}\int \frac{h_I + sx}{h_I^2 sx}[J_1 \sin T - \{J_0 - \frac{J_1}{X}\}\cos T][J_1 \cos T + \{J_0 - \frac{J_1}{X}\}\sin T]dt \\ &-\frac{A\sigma C}{gh_I}\int \{J_0 \cos T - J_1 \sin T\}dt \end{aligned} \tag{23}$$

3.3 Radiation stress, setup, and attenuation for internal waves

During the passage of surface waves, there are mean transport of water upward the shoreline and depression of the mean water level from the still water level. Longuet-Higgins and Stewart (1964) introduced the radiation stress concept to prove these mechanisms, and Umeyama (2006) applied it to internal waves. The principal component of the radiation stress for internal waves can be defined as

$$S_{xx} = \overline{\int_{\eta_{II}}^{\eta_I + h_I} (p_I + \rho_I u_I^2)dz} - \int_0^{h_I} p_{I0}dz + \overline{\int_{-h_{II}}^{\eta_{II}} (p_{II} + \rho_{II} u_{II}^2)dz} - \int_{-h_{II}}^{0} p_{II0}dz \tag{24}$$

where S_{xx} =radiation stress for internal waves; p_{I0} =hydrostatic pressure in the upper layer; p_{II0} =hydrostatic pressure in the lower layer; and the over-bar denotes averaging in time over a wave period. Assuming that the upper limit of integration may be replaced by $z = h_I$, the displacement of the density interface is small relative to the wavelength, and the mean mass flux of vertical momentum across a horizontal plane balances with the weight of the water above it, Eq.(24) reduces to

$$S_{xx} = \int_0^{h_I} \rho_I \overline{(u_I^2 - w_I^2)} dz + \int_{-h_{II}}^{0} \rho_{II} \overline{(u_{II}^2 - w_{II}^2)} dz \tag{25}$$

Substituting Eqs.(9)-(12) into Eq.(25), the radiation stress of internal waves becomes

$$S_{xx} = \frac{a^2}{2}\{\rho_I(\frac{k^2 h_I}{\sigma^2}\alpha^2 - \sigma^2 h_I) + \frac{\rho_{II}\sigma^2 h_{II}}{\sinh^2 kh_{II}}\} \tag{26}$$

The change in radiation stress leads to a change in the mean level of the density interface when internal waves encounter a sloping beach. The equilibrium between radiation stress change and average slope of the density interface yields

$$\frac{dS_{xx}}{dx} - \{\rho_I - \rho_{II}\} g(\bar{\eta} + h_{II}) \frac{d\bar{\eta}}{dx} = 0 \tag{27}$$

Generally, the attenuation of internal waves in the continental slope is a complicated hydrodynamic process. For the purpose of the present study it may be helpful to use a model in which the divergence of the energy flux is balanced by the dissipation. Therefore, the equation of energy conservation can be expressed as (Umeyama & Shintani 2006)

$$\frac{dF}{dx} = \frac{d(EC_g)}{dx} = -f_w \frac{\rho_I + \rho_{II}}{3\pi}(\frac{\sigma a}{\sinh kh_{II}})^3 - \beta \frac{(\rho_I + \rho_{II})g}{4\pi\sqrt{2}}\sigma a^2 \tag{28}$$

where F =energy flux per unit of width; E =depth-integrated, time-averaged wave energy per unit area; f_w =friction coefficient; and β =energy dissipation coefficient.

3.4 Theoretical water particle trajectory

In the case of internal waves on a slop, we denote $(x_I(t), z_I(t))$ and $(x_{II}(t), z_{II}(t))$ the instantaneous water particle positions at time t in the upper and lower layers, respectively. The corresponding horizontal and vertical velocities become $u_I = \partial x_I / \partial t$, $w_I = \partial z_I / \partial t$, $u_{II} = \partial x_{II} / \partial t$, and $w_{II} = \partial z_{II} / \partial t$. When the mean position of a water particle is given at $(\overline{x_I}, \overline{z_I})$ for the upper layer or at $(\overline{x_{II}}, \overline{z_{II}})$ for the lower layer, the instantaneous water particle position is denoted as $x_I(t) = \overline{x_I} + \varsigma_I(t)$ and $z_I(t) = \overline{z_I} + \xi_I(t)$, or $x_{II}(t) = \overline{x_{II}} + \varsigma_{II}(t)$ and $z_{II}(t) = \overline{z_{II}} + \xi_{II}(t)$, where ς_I, ξ_I and ς_{II}, ξ_{II} are the horizontal and vertical displacements in the upper layer and lower layer, respectively. Thus, expansion of velocities in the Taylor series and integration of those velocities with respect to time yield

$$\begin{aligned}\varsigma_I = {} & \frac{A^2 C}{2\sigma h_I}\frac{h_I + sx}{h_I sx}\{-J_1^2(\frac{T}{2} + \frac{\sin 2T}{4}) + J_1 J_{01}\frac{\cos 2T}{2} + J_{01}^2(-\frac{T}{2} + \frac{\sin 2T}{4})\} \\ & - \frac{AC}{\sigma h_I}(J_0 \cos T - J_1 \sin T)\end{aligned} \tag{29}$$

$$\begin{aligned}\varsigma_{II} = &-\frac{A\varepsilon_g}{\sigma}\sqrt{\frac{h_I+sx}{h_I sx}}(J_1\sin T + J_{01}\cos T)\\ &+\frac{A^2\varepsilon_g^2}{\sigma^2}(\frac{h_I+sx}{h_I sx})[\frac{1}{2sx^2}\frac{h_I sx}{h_I+sx}(J_1^2\frac{\cos 2T}{4}+J_1J_{01}\frac{\sin 2T}{2}-J_{01}^2\frac{\cos 2T}{4})\\ &-J_1J_{01}\frac{dX}{dx}\frac{\cos 2T}{4}+J_0\{J_1\frac{dX}{dx}-\frac{1}{X}(\frac{1}{2sx^2}\frac{h_1 sx}{h_1+sx}J_1-J_{01}\frac{dX}{dx})\}(-\frac{T}{2}+\frac{\sin 2T}{4})\\ &-J_{01}^2\frac{dX}{dx}(\frac{T}{2}+\frac{\sin 2T}{4})-J_{01}\{J_1\frac{dX}{dx}-\frac{1}{X}(\frac{1}{2sx^2}\frac{h_1 sx}{h_1+sx}J_{01}\frac{dX}{dx})\frac{\cos 2T}{4\sigma}\}]\end{aligned} \tag{30}$$

where $J_{01} = J_0 - J_1 / X$.

4. Results

4.1 Interfacial displacement and celerity distribution

Fig.4 shows the spatial displacements of the density interface for two different experiments, i.e. (a) Case 1 and (b) Case 2. The interval between two panels is $T/4$ for each case. The abscissa is the distance from the intersection between the sloping bed and stationary level of the density interface, and the ordinate is the elevation above that level. The circular symbols show the density interface by using the image processing technique. The solid curve shows the analytical solution based on Eq.(19). For Case 1, the absolute value of the crest level is larger than that of the trough level, and this tendency is prominent in the upper-slope region. Inspecting the four figures reveals that the test data agree with the theoretical displacement in the horizontal range of $15 < x < 50$ cm. To obtain closer agreement in the rest of range, several appropriate assumptions such as breaking, bottom friction, reflection and return flow may be proposed to account for the observed wave profiles. For Case 2, the experimental waveform is peaked near the crest but declined near the trough except in the upper-slope region, when comparing it to the theoretical profile. The method of characteristics appears to adequately predict the details of the runup profile on the sloping bottom. Umeyama and Shintani (2006) examined the similar measured distributions with the $k-\varepsilon$ model and the method of characteristics, and found that the former is quantitatively superior to the latter in the upper-slope region.

Fig.5 depicts the corresponding variations of celerity for Cases 1 and 2. The celerity distributions obtained from the linear wave theory (Eq.14) and the method of characteristics by Umeyama & Shintani (2004) are presented to compare with the experimental data. The measured celerity is smaller than these predicted ones except in the upper-slope region where most measured values exceed the predicted ones by the linear wave theory for Case 1 and those by the method of characteristics for Case 2. In the present cases, i.e. the linear bottom slope of 3:50, the solution by the linear wave theory shows a fair agreement with the measured celerity when compared with the solution by the method of characteristics. According to Umeyama and Shintani (2006), the former underestimates the measurements but the latter overestimates them by about 0-30% in some experimental cases for the bottom slope of 1:28. These quantitative discrepancies could be due to the difference of boundary conditions of the experiment and the theory. The theoretical solution was derived for a topography consisting of a plane sloping beach, although the experimental data were

obtained over a different topography consisting of a constant depth between 0 and 100 cm from the wavemaker and a slope between 100 and 600 cm from it.

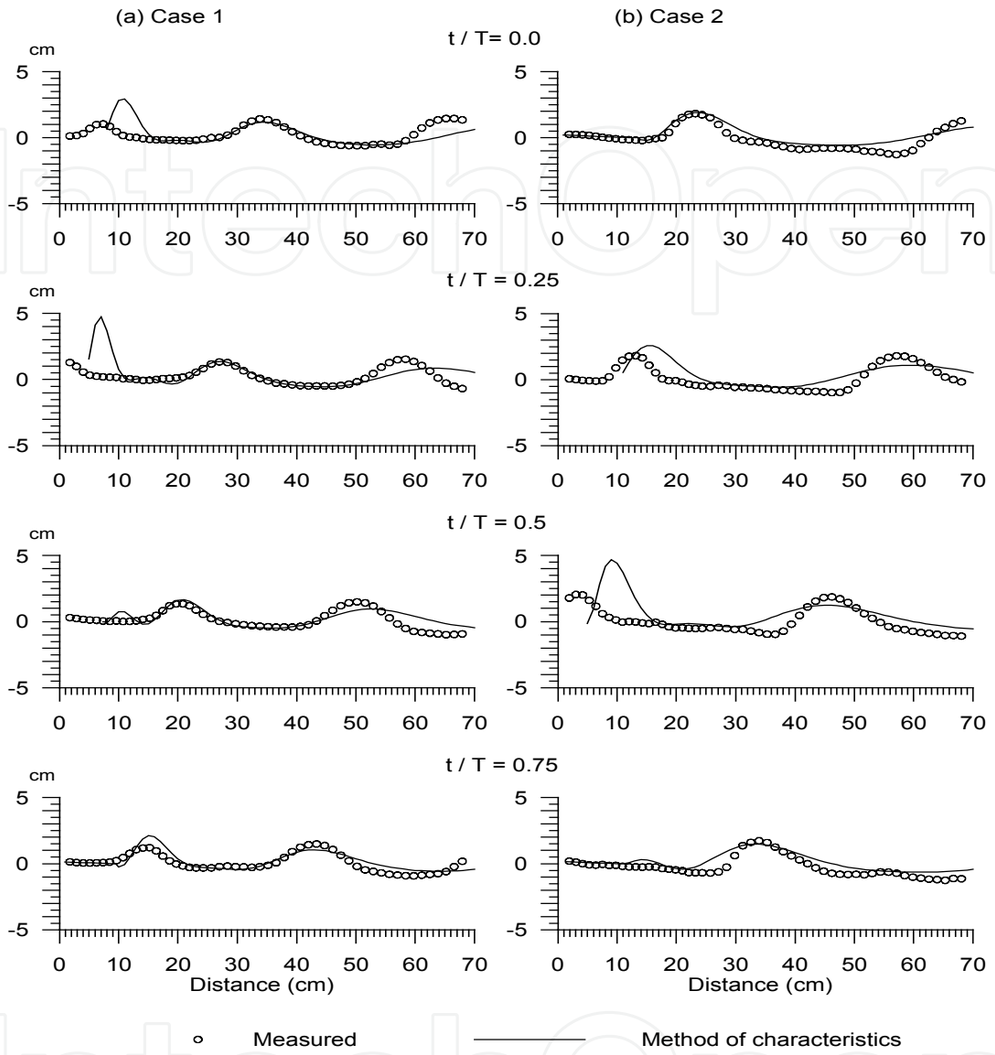

Fig. 4. Spatial displacements of density interface of $h_I : h_{II}$ =15 cm:15 cm

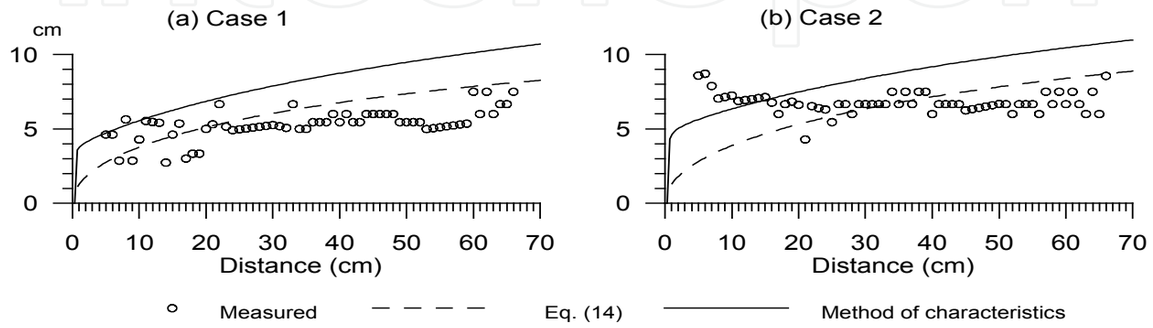

Fig. 5. Spatial profiles of celerity

4.2 Attenuation and setup for internal waves

The laboratory data in this section were obtained for the upper and lower thickness ratio of $h_I : h_{II}$ = 15 cm:15 cm. Fig.6 represents a series of temporal displacements of the density interface for Case 1 at six horizontal locations along the wave tank. All waveforms differ considerably from a sinusoidal profile, but the general characteristics at any given location are quite similar. The interfacial displacements show strong nonlinearity. These internal waves exhibit a higher rise at the crest and a depression near the trough in the upper-slope region. When waves are moving closer to the origin, a prominent feature of the cnoidal-type fluctuations continues from one wave to the next. The wave height abruptly decreases, while its mean density interface slowly increases.

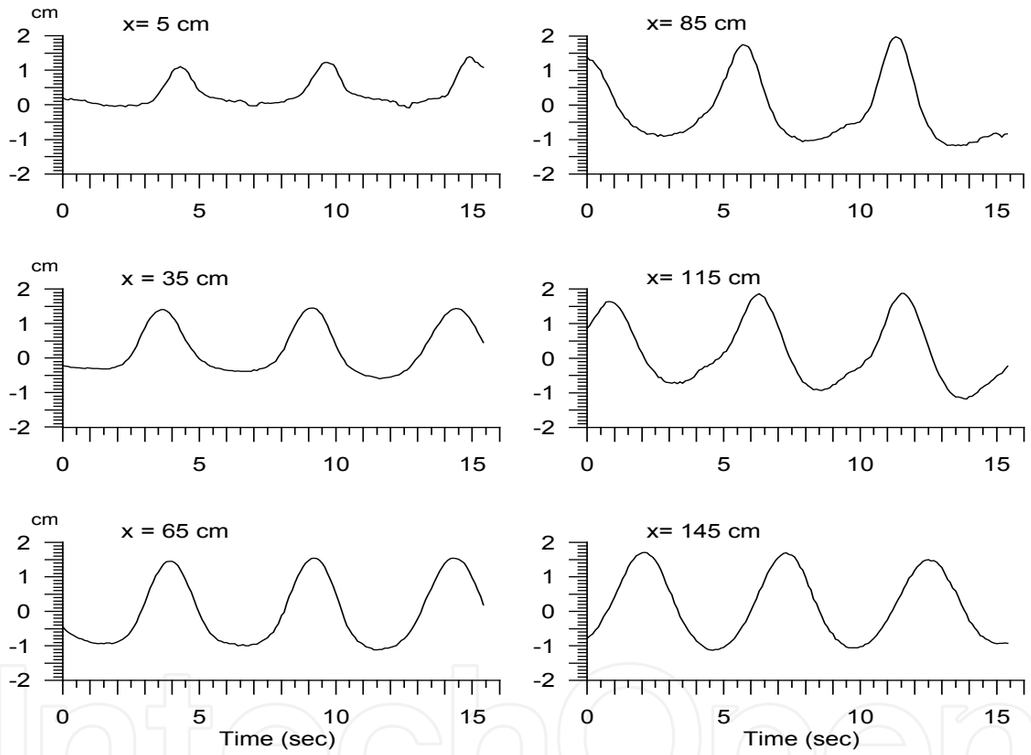

Fig. 6. Temporal displacement of density interface for Case 1

Fig.7 shows comparisons of predicted and observed variations of the local wave height and the mean density interface for Cases 1 and 2. Illustrated in the solid curve are the wave transformation predicted using Eq.(28) and the wave setup or set-down using Eq.(27). A portion of the incident wave motion is converted to the forward translation of the water mass by the breaking process. This results in forming a bolus that runs further up the face of the slope. The maximum runup elevation depends on the wave steepness and the bottom angle. Although the reflection coefficient should be determined in advance of the calculations of attenuation and setup, the reflection was neglected. In order to calculate the wave-height distribution, the value of β in Eq.(28) was determined using a trial-and-error procedure. In the present computation, it was equal to 0.020 for Case 1 and 0.025 for Case 2.

For shoaling waves on a given bottom slope, the wave height decreases gradually with decreasing water depth but does not vanish at the origin. Good agreement is found between the measured and calculated values of wave height in the recorded region. The discrepancy between these measured and calculated distributions is probably due to the neglect of the reflection or the overestimation of shear stress parameters. The radiation stress for partial standing waves differs from that for incident waves; it is presented by the sum of the incident and reflected waves. For surface waves, Longuet-Higgins and Stewart (1964) found that the mean surface level for a standing wave train slightly increases at the antinodes and correspondingly decreases at the nodes, having twice the frequency of an incident wave train. A somewhat similar relationship was found in the experimental result by Umeyama (2008) for partial standing internal waves. Partial standing internal waves develop a longitudinal mean interfacial oscillation that is a half period out of phase. Although it is difficult to detect these oscillations from the observation data, generally, the theoretical mean interfacial displacement agrees with the measured setup.

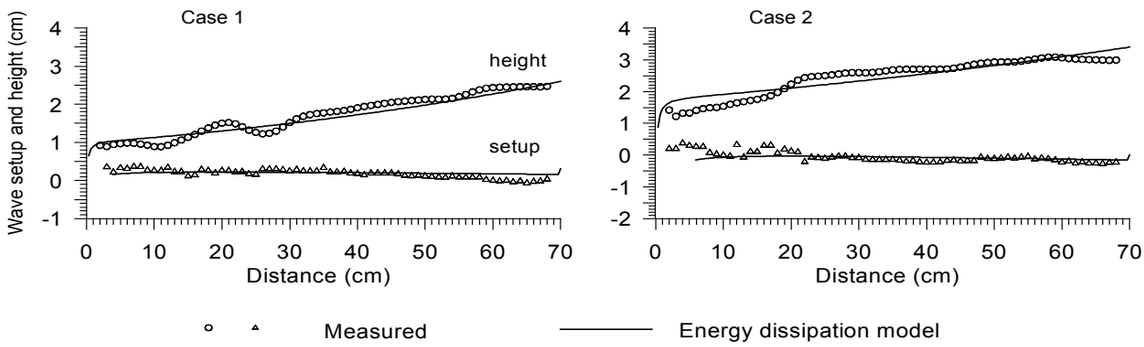

Fig. 7. Attenuation and setup of internal waves on a slope

4.3 Instantaneous velocity fields of internal waves

Fig.8 depicts the experimental velocity fields of internal waves for the layer thickness ratio of $h_I : h_{II}$ =15 cm:15 cm by a PIV measurement. Each vector image consists of two pictures taken simultaneously using two high-definition digital video cameras. Internal waves propagate from right to left. Fig.8 (a) indicates four velocity fields at an interval of $T/4$ for Case 1, in which the internal waves were generated with a period of T = 5.2 s, and the measured wave height was H =2.6 cm at a location 100 cm from the wavemaker. In these experimental images, an array of asymmetric vortices forms along the wave tank and their scale decreases as waves progress into the shallow-water region. The mean velocity in the lower layer appears to be relatively larger than that in the upper layer. The thinner clockwise vortex alternates with the thicker counterclockwise vortex, and the array of

vortices sakes vertically from the mean density interface (z =0). Although the distortion to the pair of vortices occurs in the upper slope, the velocities still show quasi-elliptical trends. Closer the density interface, the magnitude of the velocity vector reaches its maximum. The center of vortex located within a zone between the crest and trough of internal waves. Generally, the center of ellipse starts to depart upward from the density interface before the wave crest arrives, while it deviates downward slightly from the mean interface level before the wave trough arrives. The flow under the density interface converges in the front of the wave crest and diverges behind it. This contributes to creating trajectory systems in the upper and lower layers, without crossing the density interface. Fig.8 (b) depicts four velocity fields for Case 2. The clockwise and counterclockwise vortices are in an orderly line when compared with those in Fig.8 (a). This fact suggests that an increase of wave period leads to

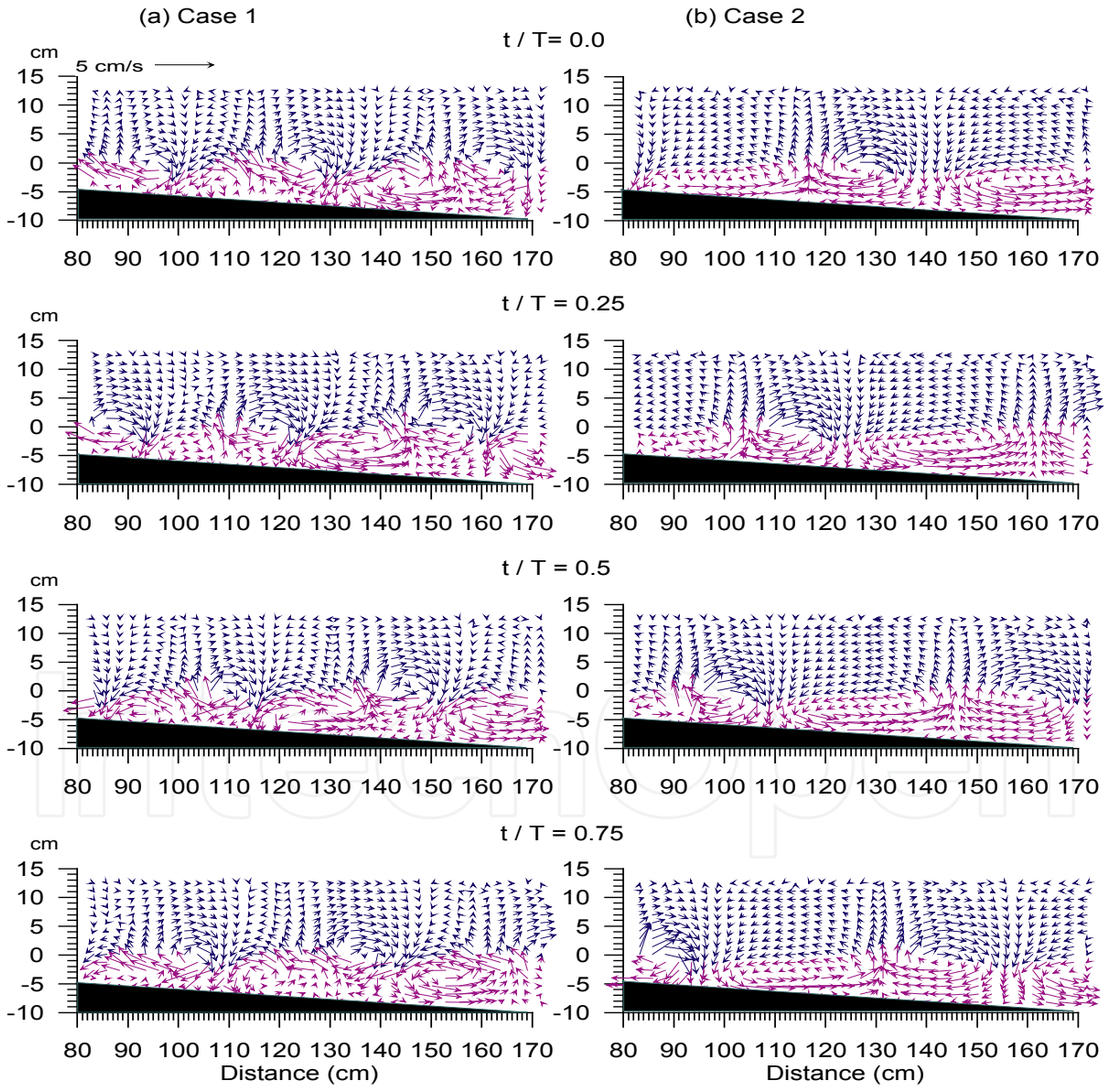

Fig. 8. Instantaneous velocity fields of internal waves ($h_I : h_{II}$ = 15 cm:15 cm)

an increase in the stability of vortices that gradually decrease the size with distance up the slope. From a pair of counterrotating vortices, one can expect the nonlinearity of internal wave, although the difference of two vertical positions for the counterrotating vortices is relatively small. The flow is no more symmetric with respect to the vertical line at the node in these cases.

Fig.9 shows a similar comparison for the generated internal waves in the density-stratified water where the upper and lower thickness ratio is $h_I : h_{II}$ = 10 cm:20 cm (Cases 3 and 4).

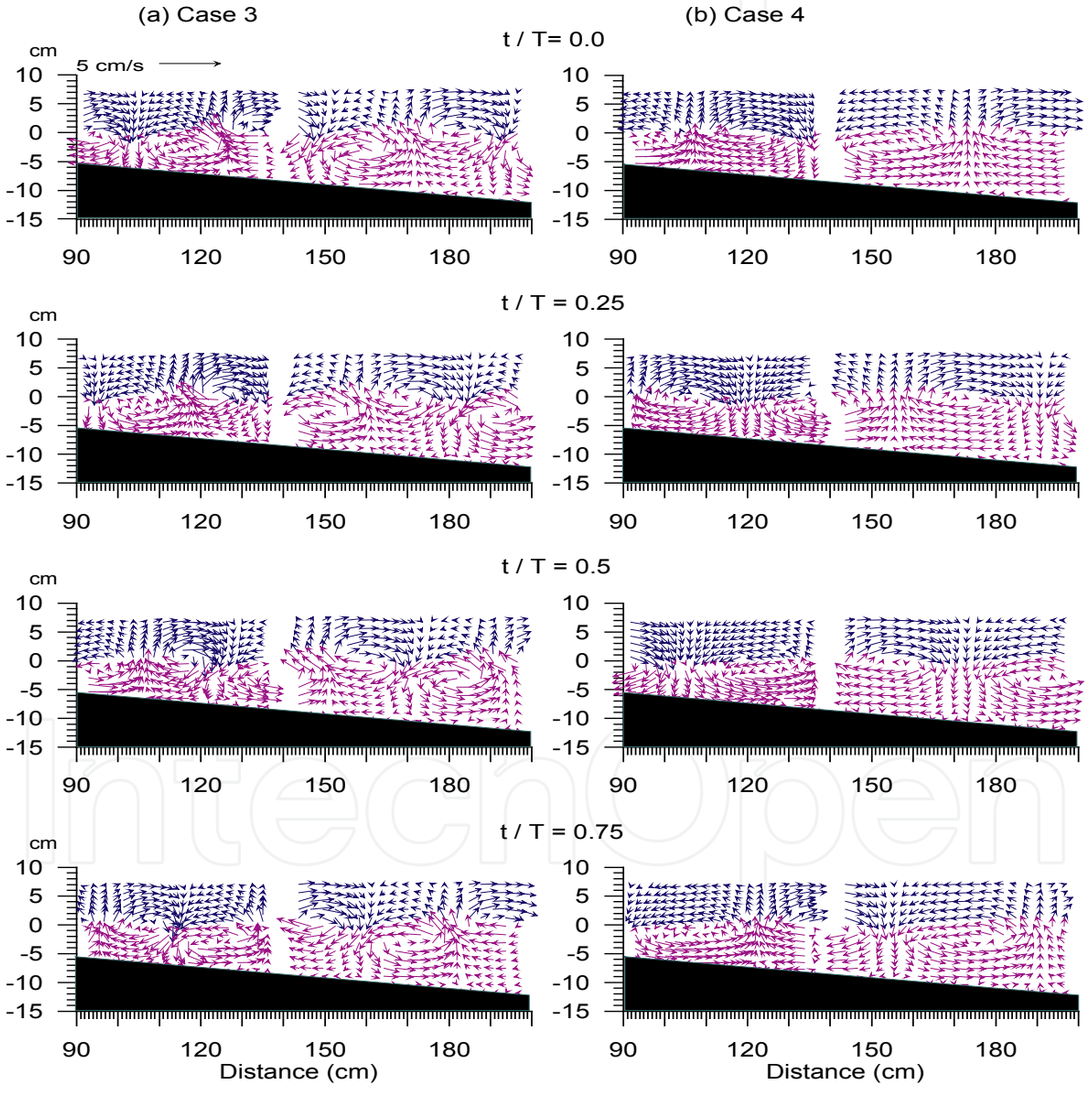

Fig. 9. Instantaneous velocity fields of internal waves ($h_I : h_{II}$ = 10 cm:20 cm)

The experimental data points are missing due to the flume flange in the range of 135 cm< x <145 cm. A pair of counterrotating vortices in the experiment shows still a satisfactory pattern. Umeyama & Matsuki (2011) found that the vortex pair turns inconspicuous by changing the thickness rate from $h_I : h_{II}$ =15 cm:15 cm to $h_I : h_{II}$ =5 cm:25 cm in a fluid of finite depth over a flat bed. The present improvement may be attributed to the replacement of the PIV system from two frequency doubled Nd:YAG lasers of 50-mW energy to a frequency-doubled Nd:YAG laser of 8-W energy. It could be confirmed from a series of experiments that the water particle movement in clockwise vortices is stretched in the horizontal direction while the anticlockwise vortices become less elliptical in the longitudinal direction over the slope.

4.4 Vertical distributions of velocity components

In this section, the measured profiles of the horizontal and vertical components of velocity at a cross-section are examined. An example of these profiles is shown in Fig.10 for Case 2.

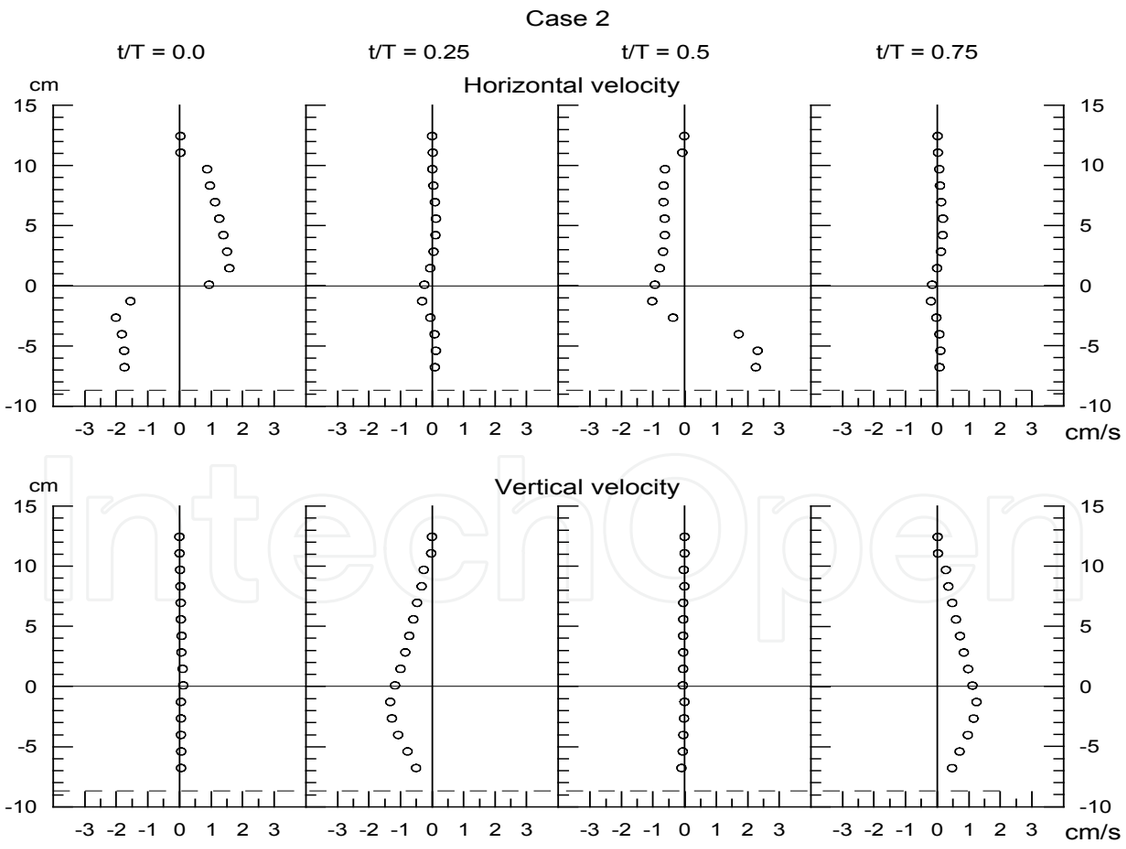

Fig. 10. Vertical distributions of velocity components at x =145 cm for Case 2

The PIV data at x =145 cm are exhibited individually for four different phase values: i.e., t/T =0.0, 0.25, 0.5, and 0.75. The horizontal solid line indicates the density interface, while the dash line indicates the bottom at this cross-section. The wave direction is from right to left in the horizontal velocity panel. The time-marching exhibitions were performed to examine the application of the PIV method to the velocity variations in a total depth. Under the crest of an internal wave at t/T =0.0, the vertical velocity is nearly zero over the depth. The horizontal velocity in the wave direction appears in the total lower layer, and reaches the maximum slightly below the wave trough level ($z \approx -2.0$ cm). In the upper layer, the horizontal velocity is opposed to the wave direction. It increases from the density interface until the wave crest level $z \approx -1.0$ cm, and slowly decreases to the surface. Under the node of an internal wave at t/T =0.25, the upward velocity starts to increase from the bottom,

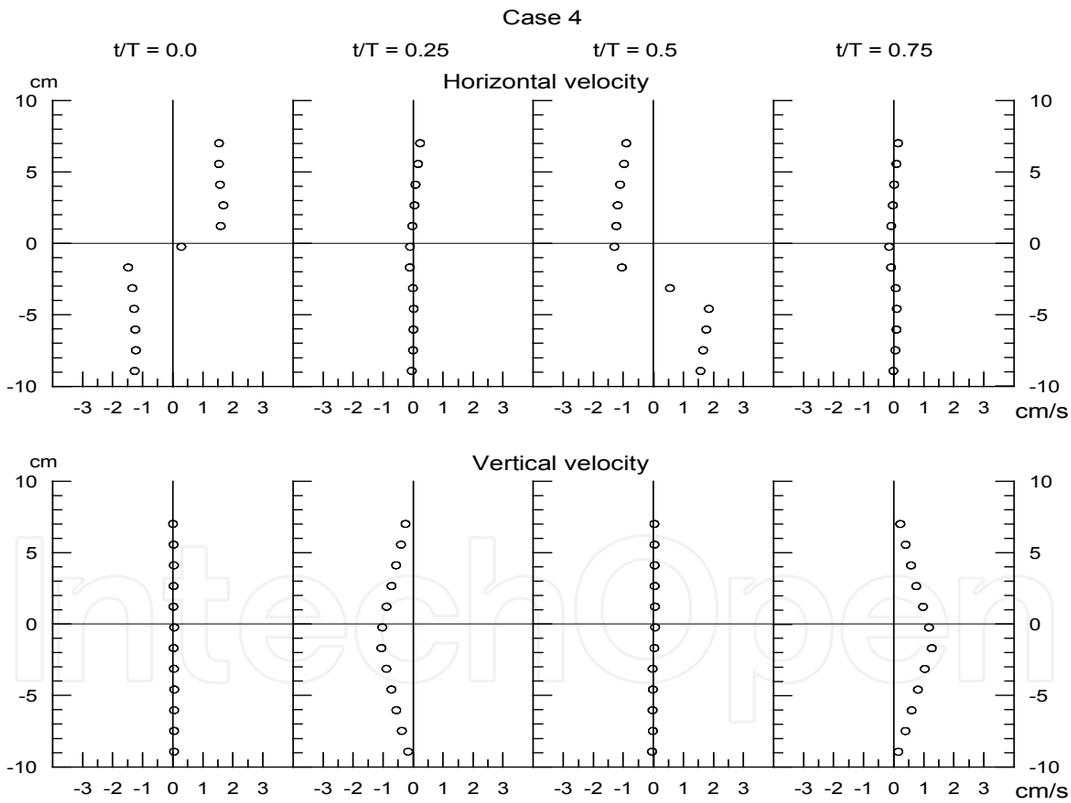

Fig. 11. Vertical distributions of velocity components at x =170 cm for Case 4

becomes the peak at an elevation slightly below the density interface, and decreases to the surface. The horizontal velocity is zero except in the region where there is a slight rise of velocity in the wave direction near the density interface. Under the trough at t/T =0.5, the direction of horizontal velocity changes in the lower layer. The velocity peak occurs at $z \approx -1.0$ cm in the wave direction and $z \approx -5.5$ cm in the direction opposing to the wave. The velocity decreases slowly toward the surface in the upper layer but it keeps a relatively large value at the bottom. Under the other node at t/T =0.75, the downward velocity dominants the phase. The vertical velocity profile is reverse to that at t/T =0.25. The horizontal velocity in the wave direction can be only found in the region from -1.0 cm $\le z \le 0.0$ cm.

Fig.11 depicts similar distributions of the horizontal and vertical components of velocity for Case 4, in which the experiment was performed for the layer thickness ratio of $h_I : h_{II}$ =10 cm:20 cm. Plotted are two velocity components at x =170 cm. Under the crest and trough, the horizontal velocities are maxima, while the vertical velocities are zero, and under the nodes, the opposite is true. At t/T =0.0 and 0.5, the horizontal velocity decreases slowly to the surface in the upper layer or the bottom in the lower layer but does not vanish near these boundaries. In contrast, the horizontal velocity is zero over the depth at t/T =0.25 and 0.75 when the velocity peak in the vertical direction appears slightly below the mean density interface.

4.5 Water particle trajectories

Fig.12 displays a plot of the particle orbit geometries for $h_I : h_{II}$ = 15 cm:15 cm and $h_I : h_{II}$ = 10 cm:20 cm. Shown in the diagram are attained for four wave conditions: i.e. (a) Case 1; (b) Case 2; (c) Case 3; and (d) Case 4. The data were taken approximately at the center of the frame in the digital video camera. The circular symbol indicates the instantaneous position of a water particle based on the PIV technique in which each Lagrangian point was determined using the present algorithm (see Fig.3). All trajectories are not elliptical and not closed for each case. Near the density interface in the lower layer, the horizontal and vertical displacements of the water particle are large relative to those near the mid-depth and surface region. The particle tends to take less distance to complete one wave cycle in the wave direction for larger wave period. Generally, the vertical excursion of the particle becomes smaller than its horizontal excursion with distance up in the water column. At these elevations, the particle moves backward from the wave direction to maintain a balance between the following and opposing fluxes in the wave tank. In contrast, the particle marches forward in a large nonclosed loop at the density interface, implying that each particle has a periodic motion per wave cycle but yields a maximum forward drift. The horizontal particle displacement in the direction opposing to the wave propagation increases with distance down in the water column for Cases 3 and 4. Fig.13 shows the theoretical trajectory calculated for Cases 1, 2, 3, and 4 by equations (19), (29) and (30) whose higher terms lead to an asymmetry of the particle orbit. Note that ideal trajectory data cannot be obtained without removing extraneous effects such as reflection from the wall and higher harmonics generated by the wavemaker, although the size of the wave tank restricts these effects. Inspecting the present comparisons for internal waves, however, the experimental path is qualitatively in good agreement with the theoretical trajectory just above and below the density interface.

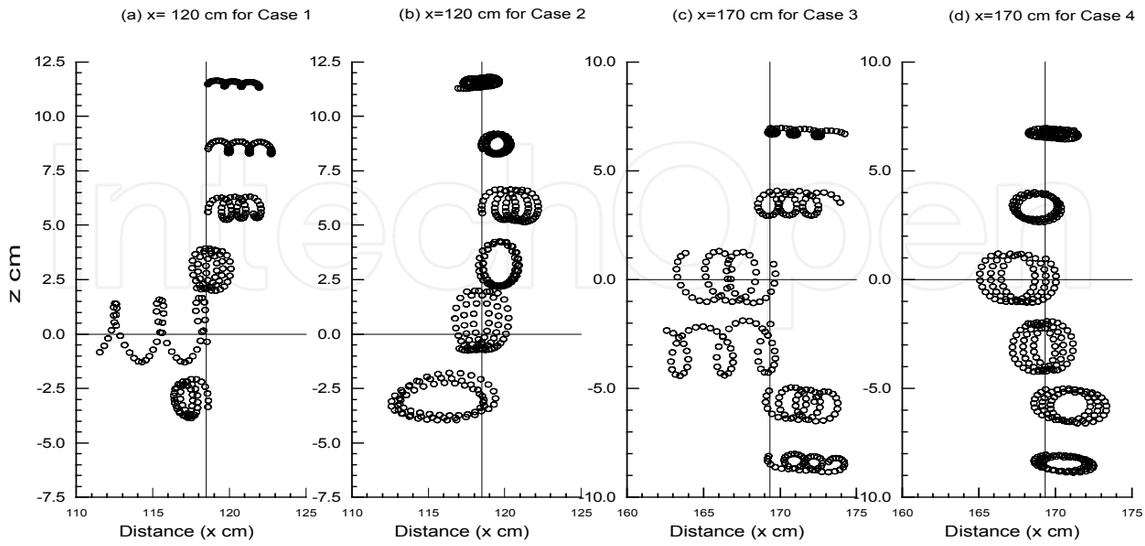

Fig. 12. Water particle trajectories by PIV/PTV method

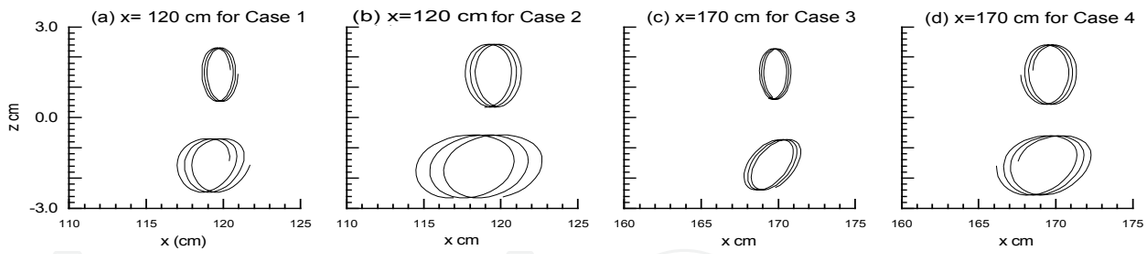

Fig. 13. Calculated particle paths by the Method of characteristics

5. Conclusion

In the present study, an image processing technique was used to quantify the spatial and temporal displacements of the density interface, and a PIV system was examined to illustrate the velocity fields in layers of fresh and salt water over a slowly varying water depth. The wave generation was made by a slide-type wavemaker. Wave celerity, attenuation and setup of internal waves were investigated theoretically and experimentally. The method of characteristics was adapted to express the internal waves at the interface of two fluids of slightly different densities on a sloped topography. A comparison of theoretical and measured variations of internal waves indicated that the agreement with

these values improves when the target area is located in the region slightly apart from the origin. Over the range of interest, the spatial variations of internal waves were well predicted by the nonlinear long-wave equation. In addition, the wave celerity was obtained by analyzing the experimental data and compared with the result by the method of characteristics. To predict the local wave-height attenuation and the setup of density interface, we used the energy dissipation model, the energy conservation equation, and the momentum balance equation based on the radiation stress concept for internal waves by Umeyama and Shintani (2006). Note that the spatial variations of wave height and setup for all experimental conditions were well reproduced by the theoretical solution.

Using a PIV system, we measured the water particle velocity to obtain successive velocity fields over one wave cycle. The instantaneous velocity vector map clearly illustrated a vortex pair when the thickness ratio was relatively large in a fluid of two density layers. The vertical distributions of velocities analyzed from the PIV data were also presented at different phases. In addition to the common use of the PIV technique, we extended the knowledge to the visualization of the mass transport due to the propagation of internal waves. The algorithm for PIV was employed to compute Lagrangian velocity and track water particle displacements in Eulerian grids. The particle trajectories in a cross-section were simulated using a solution based on the definition of the Lagrangian approach to the method of characteristics. The agreement between the computed and measured results near the density interface was reasonable, apart from the restriction resulting from the apparatus. Thus, the proposed approach of the PIV can be applied to the Lagrangian description of the trajectory of a water particle when internal waves propagate above a sloping bottom.

6. Acknowledgment

The authors wish to thank Shinya Watanabe, Yasuhiro Takei and Ryota Kobayashi for preparing all experimental data.

7. References

Apel, J. R., Byrne, H. M., Proni, J. R., and Charnell, R. L. (1975). Observations of oceanic internal and surface waves from the earth resources technology satellite. *J. Geophys. Res.*, Vol.80, No.6, pp.865–881, ISSN: 0148–0227.

Apel, J. R., Byrne, H. M., Proni, J. R., and Sellers, R. L. (1976). A study of oceanic internal waves using satellite imagery and ship data. *Remote Sens. Environ.*, Vol.5, pp.125–135, ISSN: 0034-4257.

Apel, J. R., Holbrook, J. R., Liu, A. K., and Tsi, J. (1985). The Sulu Sea internal soliton experiment. J. Phys. Oceanogr., Vol.15, No.12, pp.1625–1651, ISSN: 0022-3670.

Austin, R.W. and Halikas, G. (1976). "The index of refraction of seawater." Scripps Institution of Oceanography, Ref. No. 76-1.

Grue, F., Jensen, A., Rusas, P.-O. and Sveen, J.K. (1999). Properties of large-amplitude internal waves. *J. Fluid Mech.*, Vol.380, pp.257-278, ISSN: 0022-1120.

Grue, F., Jensen, A., Rusas, P.-O. and Sveen, J.K. (2000). Breaking and broadening of internal solitary waves. *J. Fluid Mech.*, Vol.413, pp.181-217, ISSN: 0022-1120.

Helfrich, K. R. (1992). Internal solitary wave breaking and run-up on a uniform slope. *J. Fluid Mech.*, Vol.243, pp.133–154, ISSN: 0022-1120.

Helland-Hansen, B., and Nansen, F. (1926). The eastern North Atlantic. *Geofys. Publ.*, Vol.4, No.2.

Kao, T. W., Pan, F.-S., and Renouard, D. (1985). Internal solitons on the pycnocline: Generation, propagation, and shoaling and breaking over a slope. *J. Fluid Mech.*, Vol.169, pp.19-53, ISSN: 0022-1120.

LaFond, C. (1962). Internal waves, Part 1, In: *The sea*, M. N. Hill, ed., Interscience, New York, 1, pp.731–751.

Longuet-Higgins, M. S., and Stewart, R. W. (1964). Radiation stress in water waves: A physical discussion, with applications. *Deep-Sea Res.*, Vol.11, pp.529–562, ISSN: 0967-0637.

Michallet, H., and Ivey G. N. (1999). Experiments on mixing due to internal solitary waves breaking on uniform slopes. *J. Geophys. Res.*, 104(C6), pp.13467-13477, ISSN: 0148–0227.

Shand, J. A. (1953). Internal waves on Georgia Strait. *Trans.*, AGU, Vol.34, No.6, pp.849–856.

Shimizu, R., Shintani, T. and Umeyama, M. (2005). Instantaneous and Lagragian velocity fields of internal waves on a slope by PIV measurement and numerical simulation. Annu. *J. Coastal Eng.*, Vol.52, pp.1-5.

Thorpe, S. A. (1968). On the shape of progressive internal waves. *Phil. Trans. the Royal Soc. A*, Vol.263, pp.563–614, ISSN: 1471-2962.

Umeyama, M. (2002). Experimental and theoretical analyses of internal waves of finite amplitude. *J. Waterway, Port, Coastal, and Ocean Eng.*, ASCE, Vol.128, No.3, pp.133-141, ISSN:0733-950X.

Umeyama, M. (2008). PIV techniques for velocity fields of internal waves over a slowly varying bottom topography. *J. Waterway, Port, Coastal, and Ocean Eng.*, ASCE, Vol.134, No.5, pp.286-298, ISSN:0733-950X.

Umeyama, M. (2011). Coupled PIV and PTV measurements of particle velocities and trajectories for surface waves following a steady current. *J. Waterway, Port, Coastal, and Ocean Eng.*, ASCE, Vol.137, No.2, pp.85-94, ISSN:0733-950X.

Umeyama, M. (2012). Eulerian/Lagrangian analysis for particle velocities and trajectories in a pure wave motion using particle image velocimetry. *Phil. Trans. the Royal Soc. A*, 370(1964), pp.1687-1702, ISSN: 1471-2962.

Umeyama, M. and Matsuki, S. (2011). Measurements of velocity and trajectory of water particle for internal waves in two density layers. *Geophysical Res. Lett.*, AGU, Vol.38, No.3, L03612.

Umeyama, M. and Shinomiya, H. (2009) Particle image velocimetry measurements for Stokes progressive internal waves. *Geophysical Res. Lett.*, AGU, Vol.36, No.6, L06603.

Umeyama, M. and Shintani, T. (2004). Visualization analysis of runup and mixing of internal waves on an upper slope. *J. Waterway, Port, Coastal, and Ocean Eng.*, ASCE, Vol.130, No.2, pp.89-97, ISSN:0733-950X.

Umeyama, M. and Shintani, T. (2006). Transformation, attenuation, setup and undertow of internal waves on a gentle slope. *J. Waterway, Port, Coastal, and Ocean Eng.*, Vol.132, No.6, pp.477-486, ISSN:0733-950X.

Umeyama, M., Shintani, T. and Watanabe, S. (2011). Measurements of particle velocities and trajectories in a wave-current motion using PIV and PTV. *Proceedings of 32nd Inter. Conf. of Coastal Eng.*, ASCE, ISSN: 2156-1028, Shanghai, July, 2010.

Walker, S. A., Martin, A. J., Easson, W. J., and Evans, W. A. B. (2003). Comparison of laboratory and theoretical solitary wave kinematics. *J. Waterway, Port, Coastal, and Ocean Eng.*, ASCE, Vol.129, No.5, pp.210–218, ISSN:0733-950X.

Wallace, B. C., and Wilkinson, D. L. (1988). Run-up of internal waves on a gentle slope in a two-layered system. *J. Fluid Mech.*, Vol.191, pp.419–442, ISSN: 0022-1120.

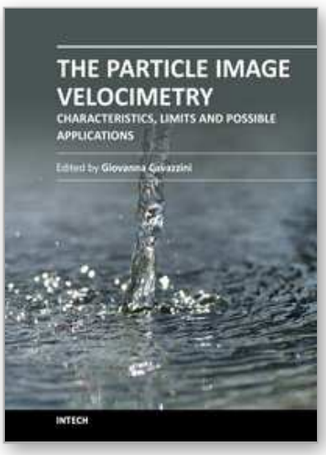

The Particle Image Velocimetry - Characteristics, Limits and Possible Applications

Edited by PhD. Giovanna Cavazzini

ISBN 978-953-51-0625-8
Hard cover, 386 pages
Publisher InTech
Published online 23, May, 2012
Published in print edition May, 2012

The Particle Image Velocimetry is undoubtedly one of the most important technique in Fluid-dynamics since it allows to obtain a direct and instantaneous visualization of the flow field in a non-intrusive way. This innovative technique spreads in a wide number of research fields, from aerodynamics to medicine, from biology to turbulence researches, from aerodynamics to combustion processes. The book is aimed at presenting the PIV technique and its wide range of possible applications so as to provide a reference for researchers who intended to exploit this innovative technique in their research fields. Several aspects and possible problems in the analysis of large- and micro-scale turbulent phenomena, two-phase flows and polymer melts, combustion processes and turbo-machinery flow fields, internal waves and river/ocean flows were considered.

InTech Europe
University Campus STeP Ri
Slavka Krautzeka 83/A
51000 Rijeka, Croatia
Phone: +385 (51) 770 447
Fax: +385 (51) 686 166
www.intechopen.com

InTech China
Unit 405, Office Block, Hotel Equatorial Shanghai
No.65, Yan An Road (West), Shanghai, 200040, China
中国上海市延安西路65号上海国际贵都大饭店办公楼405单元
Phone: +86-21-62489820
Fax: +86-21-62489821

IntechOpen